Thermal and mechanical properties of crack-designed thick lanthanum zirconate coatings

Sophie B. Weber, Hilde L. Lein, Tor Grande, and Mari-Ann Einarsrud[1]

Department of Materials Science and Engineering, Norwegian University of Science and Technology, N-7491 Trondheim, Norway

Abstract

Vertical cracks are beneficial in thermal barrier coatings due to enhanced thermo-mechanical compliance. Accordingly, an aqueous nitrate based precursor solution was atomized on stainless steel substrates by spray pyrolysis to deposit thick crack-designed lanthanum zirconate coatings. Coatings with designed crack patterns were deposited and characterized by electron microscopy, tribology, Vickers indentation, and thermal diffusivity. The crystallization of the coatings was investigated by *in situ* high temperature X-ray diffraction. The green coatings crystallized from 600 °C and the pyrochlore structure was formed after heat treatment at 1000 °C. Crystalline lanthanum zirconate multilayered coatings with small crack spacing and crack opening exhibited a higher density, a higher hardness, lower thermal diffusivities, and higher thermal conductivities compared to crystalline monolayered coatings of similar thickness with large crack spacing and crack opening. The thermal diffusivity of the coatings, ~28 mm^2/s at room temperature, was similar to the values reported for yttria-stabilized zirconia plasma sprayed coatings.

[1] *Author to whom correspondence should be addressed. e-mail: mari-ann.einarsrud@material.ntnu.no

Keywords

Lanthanum zirconate; Spray pyrolysis; Thermal barrier coating

1. Introduction

Thermal barrier coatings (TBCs) have been developed to increase the operating temperatures and the lifetime of gas turbine engines performing in high temperature, oxidative, and hot corrosive environment [1]. State-of-the-art TBCs consist of a ~50 μm thick NiCoCrAlY bond-coat and a porous 100-200 μm thick yttria stabilized zirconia (YSZ) top layer [2]. The ceramic top layer of a material with a low thermal conductivity induces a temperature drop across the layer of up to 170 °C, reducing the temperature at the surface of the nickel based superalloy [3]. The intermediate bond-coat provides an adherent surface for the top coat, and an oxidation and hot corrosion resistant layer to protect the underlying metallic surface. YSZ is so far the material of choice due to the low thermal conductivity and the relatively high thermal expansion coefficient compared to other ceramic materials, which reduces the thermal expansion mismatch with the bond coat [4; 5]. However YSZ has a limited operation temperature at ~1200 °C for long-term applications because of the detrimental phase transformation from the tetragonal to the monoclinic polymorph [6]. Among new promising TBC materials, lanthanum zirconate ($La_2Zr_2O_7$) is currently investigated due to its high thermal stability, low thermal conductivity, and low sintering rate [7].

The performance of commercial TBCs is highly dependent on the deposition techniques, air plasma spray (APS) and electron-beam physical vapor deposition (EBPVD) methods, which give different microstructures leading to different thermal

and mechanical properties of the ceramic coating. EBPVD produces a columnar microstructure with elongated intercolumnar pores aligned normal to the superalloy surface, increasing the compliance of the coating [8]. However, the orientation of the EBPVD pores does not reduce the thermal conductivity of the coating [9]. TBCs deposited by APS consist of "splat" grains with inter-"splat" pores and micro-cracks parallel to the surface of the substrate [10]. The aligned pores, oriented normal to the heat flow, reduce the thermal conductivity of the layer, but at the expense of the spallation life of the coating [11]. To improve the lifetime of TBCs deposited via APS by improving the strain tolerance, dense vertical cracks (DVCs) were introduced in the coatings [12]. However, for coatings with a density of less than 88 % of theoretical, DVCs do not form and improved compliance is obtained to the detriment of the low thermal conductivity [13].

Furthermore, nanostructured TBCs are proposed to give superior wear resistance and lower thermal conductivity compared to conventional coatings [14]. Nevertheless, with the current commercial deposition methods, which use micrometer range particles as the feedstock, uniform nanostructured TBCs are quite challenging to achieve. Recently, solution precursor plasma spray (SPPS) technique was developed to take advantage of using a liquid precursor as feedstock to deposit nanostructured coatings [15]. A typical coating deposited by SPPS consists of ultra-fine splats, through thickness vertical cracks, embedded un-pyrolized particles, and uniformly dispersed nanopores, which generate coatings with low thermal conductivity and improved durability [16]. However, APS, SPPS, and EBPVD technologies remain expensive and complex [17], especially when compared to cost-effective wet chemistry deposition methods, for

which liquid precursors also offer the possibility to better tailor the coating composition and to facilitate the deposition of doped, multilayered, or graded coatings [18].

Spray pyrolysis is of special interest due to its simplicity and versatility [19]. By air atomizing a precursor solution on a heated substrate, thin or thick films or coatings can be deposited and, by adjusting the process parameters, the microstructure can be tailored. In particular, the substrate temperature has a significant influence on the film formation [20; 21], and the deposition of thick crack-free coatings by spray pyrolysis of an aqueous precursor solution is only possible in a suitable substrate temperature interval corresponding to the deposition of ionic salt precipitates [22]. Further cracking of thick coatings occurs during the decomposition of the precursor salts in the deposited coatings due to the associated volumetric shrinkage. The effect of the deposition parameters on the crack pattern of thick coatings produced by spray pyrolysis has been investigated, and general guidelines were given to deposit coatings with engineered crack pattern. The crack spacing and the crack opening increase linearly with increasing thickness of the layer to decompose [23], hence, by depositing and decomposing layers of various thicknesses, thick mono- or multi-layered coatings with tailored crack patterns might be formed.

Besides, TBCs manufactured by the sol-gel route exhibiting similar crack networks as TBCs produced by spray pyrolysis have shown promising results in terms of durability under cyclic oxidation [24]. Nevertheless, to the authors' knowledge, the crack pattern of TBCs has not been optimized to enhance the mechanical and thermal properties.

Thus, this work aims to deposit thick nanostructured lanthanum zirconate ceramic coatings with designed crack patterns on stainless steel substrates by spray pyrolysis. The resulting coatings were characterized in terms of microstructure, thickness, thermal

and mechanical properties, as well as phase evolution with regards to the different crack patterns.

2. Experimental details

2.1. Preparation of the coatings

Zirconyl (IV) oxynitrate hydrate ($ZrO(NO_3)_2 \cdot xH_2O$; Sigma-Aldrich Gmbh, Schnelldorf, Germany, 99%) and lanthanum (III) nitrate hexahydrate ($La(NO_3)_3 \cdot 6H_2O$; Alfa Aesar Gmbh & Co., Karlsruhe, Germany, 99.9%) were dissolved in deionized water and further mixed in a molar ratio of 1:1 of La to Zr after standardization of the solutions by the thermogravimetric method. The final concentration of the precursor solution was ~0.25 mol/L.

The precursor solution was deposited at a volume flow of 1 mL/min on stainless steel (AISI 304) substrates (25 mm * 30 mm * 0.5 mm unless mentioned otherwise) previously cleaned with ethanol by a non-commercial spray pyrolysis unit developed at NTNU and described elsewhere [22]. With this setup, a precursor solution was fed to the spray unit using a peristaltic pump and further atomized on a heated substrate by a two-fluid nozzle using synthetic air (0.5 bar) as a carrier gas. The temperatures reported in the following were measured by a K-type thermocouple placed at the surface of the substrate.

In a first series of experiments, the substrate temperature was set to 240 or 280 °C, and the as-deposited coatings were further decomposed at 510, 540 or 575 °C for 14 min. The working distance between the substrate and the nozzle was 20 or 25 cm, and a volume of 10 mL was atomized. In a second series of experiments, mono- and multi-

layered coatings were deposited at 280 °C with a spraying distance of 20 cm. For the monolayered coatings, a volume of 10 mL of precursor solution was atomized, and the coating was dried for 1 min at 280 °C and further decomposed at 575 °C for 14 min. For the multilayered coatings, a volume of 2 or 5 mL was atomized, and the deposited layer was dried for 1 min at 280 °C and further decomposed at 575 °C for 2 min. This procedure was repeated according to the number of layers desired. For the final layer, the coating was dried for 1 min at 280 °C and further decomposed at 575 °C for 14 min. The decomposition of the coatings was done *in situ* with a fast heating rate between the deposition and the decomposition temperatures. The samples from both series of experiments were further heat-treated in air at 1000 or 1200 °C for 2 h.

2.2. Characterization of the coatings

The microstructures of the surface and cross-section of the coatings were analyzed using a low vacuum scanning electron microscope (SEM) (S-3400N; Hitachi, Hitachi, Japan) and a low vacuum field emission scanning electron microscope (FESEM) (Supra 55VP; Zeiss, Oberkochen, Germany). The cross-section examinations were carried out on free-standing coatings delaminated from the substrate along the cracks.

The thickness, crack spacing, crack opening and the porosity within the islands of the coatings were measured by image analysis of SEM micrographs. Crack spacing and crack opening were calculated from an average of at least forty measurements recorded *in-situ* from at least three SEM micrographs on different areas on the coatings. One measurement corresponds to the length of a line running normal to the edge of an island either toward the adjacent island for the crack openings or through the island for the crack spacing. In addition, for the crack spacing evaluation, two measurements normal

to one another were performed on each island. The porosity within the islands was estimated from binarized cross-sectional SEM micrographs using a contrast threshold to identify the ceramic coating, in white, from the pores, in black. The densities of the coatings were estimated via a mass/volume ratio using simple mass balance and geometrical considerations.

In situ high temperature X-ray diffraction (HTXRD) was performed on a green coating deposited at 280 °C on stainless steel 304 substrates (10 mm in diameter * 0.5 mm) at a distance of 20 cm using a Siemens D5005 X-ray diffractometer equipped with a Braun position sensitive detector, and using CuKα radiation. The sample was placed on a rotating alumina holder. Diffractograms were collected at room temperature, from 100 to 800 °C by steps of 100 °C and at 850 °C, maximum temperature possible using the radiant heater. The heating rate was 10 °C/min and a holding time of 360 s was maintained before starting the next measurement. Patterns were collected in the 2θ range from 10° to 85° with a step size of 0.016° 2θ. The total collection time per scan per temperature step was approximately 65 min. X-ray diffraction (XRD) of heat-treated lanthanum zirconate coatings was performed with a Bruker AXS D8 Focus diffractometer with a Lynxeye™ detector using CuKα radiation. The mean crystallite size, D, of the coatings was calculated from the most intense XRD peak (at 2θ=28.6°) in accordance with the Scherrer equation:

$$D=\frac{0.9\lambda}{\beta\cos\theta} \quad (1)$$

where λ is the X-ray wavelength used, θ and β are the diffraction angle and full-width at half-maximum of the peak, respectively.

The microhardness of the mono- and multi-layered coatings was measured using a Vickers indenter (Leica VMHT MOT; Wetzla, Germany). Each coating was indented 10 times with loads of 0.98 and 1.96 N. Due to the extent of porosity in the coatings, the hardness measurements only give the relative performance of the different coatings compared to each other.

The wear resistance of the mono- and multi-layered coatings was tested using a ball-on-disk tribometer (CSM Instruments SA; Peseux, Switzerland). A 6 mm diameter Si_3N_4 ball was used as a friction partner with 1 N load at a sliding speed of 0.5 cm/s. The coatings were examined at ambient conditions without the use of lubricant. Each measurement was conducted for 50 laps.

Finally, thermal diffusivities of a bare stainless steel substrate were measured by the laser flash method [25] using a MicroFlash™ apparatus (LFA 457; Netzsch, Selb, Germany) and the thermal diffusivities of the mono- and multi-layered coatings deposited on stainless steel substrates were calculated using a two-layer model [26] by post processing data using Netzsch LFA analysis, a software associated with the MicroFlash™ apparatus. The samples (25.4 mm in diameter) were also coated with a thin graphite layer to increase the specimen heat absorption and the wave length of the laser is 1064 nm. Measurements were recorded in a flowing N_2 atmosphere at room temperature, and from 100 to 1000 °C by steps of 100 °C. The heating rate was 10 °C/min up to 100 °C and 20 °C/min from 100 °C and up. For each temperature step, an average of three measurements recorded at 1 min interval is reported.

The thermal conductivities of the samples, λ, were then calculated using the equation (2):

$$\lambda(T) = \rho(T) \cdot C_P(T) \cdot \alpha(T) \quad (2)$$

where ρ, Cp, and α are, respectively, the density, the heat capacity, and the thermal diffusivity of the samples. The specific heat capacity of the substrate was determined by comparison of the final temperature increase of the stainless steel sample under investigation with a standard alumina sample (99.8 %; Netzsch, Selb, Germany, thickness: 0.992 mm, diameter: 25.37 mm) measured under the same conditions. The uncertainty of specific heat capacity measurements by this reference method is in the range of 10 –20 %.

3. Results

3.1. Crystallization of the coatings

First series of samples

The surface microstructures of four coatings heat-treated at 1200 °C for 2 h are shown in Fig. 1. The coatings were deposited at 240 and 280 °C at a distance of 20 and 25 cm, and decomposed at 510, 540 or 575 °C for 14 min prior to the final heat treatment. The heat-treated coatings exhibit two different crack patterns depending on the spraying distance due to the difference in thickness of the green coatings: ~70 µm for coatings sprayed at a large spraying distance and ~110 µm for coatings deposited at a small spraying distance [23]. Small crack spacing and crack opening are observed for the large spraying distance (Fig. 1(a)-(b)), and vice-versa (Fig. 1(c)-(d)). For the coatings with the smaller crack spacing and crack opening, additional cracks developed during heat treatment, and the small cracks propagated through the islands created by the

original crack pattern. Hence the crack pattern with large crack spacing and crack opening appears more stable after heat treatment compared to the one with smaller crack spacing and crack opening. X-ray diffractograms of these four coatings are displayed in Fig. 2. The lanthanum zirconate coatings are crystalline after heat treatment with the cubic pyrochlore crystal structure. However, a secondary phase of $LaMO_3$ perovskite (where M=Cr, Ni, Fe or mixtures thereof) was also detected, revealing reaction of the coatings with the substrate.

High temperature X-ray diffraction

To optimize the heat treatment temperature for the crystallization of the coatings without oxidizing the substrate, a green coating deposited at 240 °C at a distance of 25 cm was analyzed by *in situ* HTXRD, and the diffractograms are shown in Fig. 3. The coating was amorphous after deposition and crystallization to the cubic pyrochlore phase of lanthanum zirconate occurred around 600 °C. Crystalline coatings with a mean crystallite size of 12 nm were achieved at 700 °C. A secondary phase of $LaMO_3$ perovskite (where M=Cr, Ni, Fe or mixtures thereof) due to the reaction with the substrate appeared at 850 °C. The reaction with the substrate is favored by the long collection time of 65 min per scan at each temperature, and hence can be diminished by reducing heating and dwell time during the heat treatment processing step of the coatings.

3.2. Crack engineered coatings

To study the influence of the crack pattern on the thermal and mechanical properties, coatings, detailed in Table 1, with similar thickness but different crack patterns were deposited at 280 °C at a distance of 20 cm.

Monolayered coatings

Fig. 4(a)-(b) shows the surface and cross-section microstructures of a coating deposited at 280 °C and decomposed at 575 °C for 14 min. The coating was deposited in a single step, i.e. 10 mL of precursor solution were continuously atomized on the substrate to create a coating before being decomposed. The resulting coating is thick and porous, with large crack spacings and crack openings as reported in Table 1. The microstructure comprises horizontal pores to lower the thermal conductivity and vertical cracks going through the entire thickness of the coating to improve the thermo-mechanical compliance. The coating was further heat-treated for 2 h at 1000 °C and the surface and cross-section microstructures are displayed in Fig. 4(c)-(d). The microstructure of the heat-treated coating is similar to the decomposed one and, additionally, smaller cracks spread on the islands created by the large web of cracks, which explain the lower crack spacings and crack openings listed in Table 1. As seen in the insert in Fig. 4(d), the coating also exhibits a suitable porous nanostructure, and the crystallite size was calculated from Eq. (1) to be 20 nm. The bulk density of the monolayered coating was measured to be 1.57±0.02 g/cm³ corresponding to a porosity of ~74 % compared to the theoretical density. Finally, the crystal structure of the monolayered coating was the cubic pyrochlore and no reaction with the substrate was detected after heat treatment at 1000 °C for 2 h as illustrated in the lower XRD diffractogram in Fig. 5.

Multilayered coatings

Multilayered coatings with a thick bottom layer were deposited to avoid detrimental delamination previously observed for thin monolayered coatings which delaminate more significantly relative to surface after heat treatment compared to thick ones [23]. Accordingly, Fig. 6(a)-(b) shows the surface and cross-section microstructures of a four-layered coating for which 5 mL of precursor solution were deposited and decomposed to create the bottom layer, and three layers corresponding to a volume of 2 mL each were further deposited and decomposed. The resulting coating has a similar thickness as the monolayered coating with smaller crack spacing and crack opening, as summarized in Table 1. From the cross-section micrograph (Fig. 6(b)), it can be seen that successive deposition tends to partially fill in the cracks of the previous layer and that the microstructure comprises horizontal pores and vertical cracks. The four-layered coating was further heat-treated at 1000 °C for 2 h and the surface and cross-section microstructures are presented in Fig. 6(c)-(d). The microstructure of the heat-treated coating was similar to the decomposed one with similar crack spacings and crack openings. Moreover, the layered structure of the heat-treated coating seen in Fig. 6(d) also indicates that the cracks of each individual layer do not necessarily connect to form through-thickness cracks. No reaction with the substrate and a cubic pyrochlore phase were detected on the four-layered coating after heat treatment at 1000 °C for 2 h as illustrated in the upper XRD diffractogram in Fig. 5, from which the crystallite size of the porous nanostructure observed in the insert in Fig. 6(d) was calculated to be 15 nm using Eq. (1). Finally, the bulk density of this coating was measured to be 2.04±0.05 g/cm³, which represents a porosity of ~66 % compared to the theoretical density.

3.3. Mechanical properties

Hardness measurements

The hardness of crystalline mono- and four-layered coatings of similar thickness is presented in Table 2. Due to their high level of porosity, both coatings exhibit a low apparent hardness. Nevertheless, a relative comparison of the different coatings can be drawn: the four-layered coating demonstrate a higher hardness compared to the monolayered one, which is explained by the higher density. Because the volume change during decomposition is similar for both coatings and the cracks of the top layer are partially filled in during further deposition of multilayered coatings, their density is then increased compared to the monolayered ones.

Wear resistance

During the ball-on-disc test, premature failure of both coatings was observed after 2 laps, attributed to the delamination within the coatings at the boundary between the outer friction ball path and the coatings. Moreover, the circular part of the coatings which was submitted to the 1 N load via the friction was densified because of the compressive force. Densification was possible due to the high porosity and probably led to the delamination of the coatings on the outer perimeter of the friction ball path because of the large stresses generated.

3.4. Thermal properties

Thermal properties of AISI 304

To estimate the thermal properties of the coatings using a two-layer model [26], the thermal properties of the substrate must be known. The thermal diffusivity and the

specific heat capacity of a bare stainless steel substrate with a thickness of 0.51 mm were measured by the laser flash method from ambient temperature to 1000 °C. The measurements were corrected to take into account the radiation loss [27] and the finite shot pulse of the laser [28], and can respectively be fitted, in the temperature range, to the following equations:

$$\alpha_{\left[mm^2/s\right]}(T_{[K]}) = 3.824_{\left[mm^2/s\right]} + 0.0021_{\left[mm^2/K\cdot s\right]} T_{[K]} + 3.062*10^{-7}{}_{\left[mm^2/K^2\cdot s\right]} T_{[K]}{}^2 - 4.012*10^{-10}{}_{\left[mm^2/K^3\cdot s\right]} T_{[K]}{}^3 \quad (3)$$

$$C_{P[J/kg\cdot K]}(T_{[K]}) = 0.438_{[J/kg\cdot K]} + 0.0004_{\left[J/kg\cdot K^2\right]} T_{[K]} - 6.415*10^{-7}{}_{\left[J/kg\cdot K^3\right]} T_{[K]}{}^2 + 4.313*10^{-10}{}_{\left[J/kg\cdot K^4\right]} T_{[K]}{}^3 \quad (4)$$

The thermal conductivity was further calculated using Eq. (2), a density of the stainless steel substrate of 8.03 g/cm³, and the linear thermal expansion calculated from the thermal expansion coefficient reported in the literature [29]. The values were fitted, in the temperature range, to the following equation:

$$\lambda_{[W/m\cdot K]}(T_{[K]}) = 14.678_{[W/m\cdot K]} + 0.016_{\left[W/m\cdot K^2\right]} T_{[K]} - 4.329*10^{-6}{}_{\left[W/m\cdot K^3\right]} T_{[K]}{}^2 + 1.719*10^{-9}{}_{\left[W/m\cdot K^4\right]} T_{[K]}{}^3 \quad (5)$$

The measured thermal properties are in accordance with previously reported values [30], and were used in the following to evaluate the thermal properties of the deposited coatings.

Thermal diffusivity of the coatings

The thermal diffusivity measurements of the mono- and four-layered coatings were corrected in several ways. The finite shot pulse of the laser was corrected first [28]. Two different models were then applied to fit the experimental data. The first model is the two-layers adiabatic model [25], whereas the second model takes into account the heat loss of the sample [31], and the contact resistance at the interface between the coatings and the substrate [32]. In addition, due to the measurement processing, estimated thickness values of the coatings were used to perform the experiments, and the values obtained were corrected to account for the true thicknesses of the coatings. The thickness correction model is based on the adiabatic model of the laser flash method [25] and is given by:

$$\alpha_{corr} = \alpha_m \frac{t_m^2}{t_e^2} \tag{6}$$

where t_m and t_e are, respectively, the measured and the estimated thicknesses of the coatings, and α_{corr} and α_m are, respectively, the corrected thermal diffusivities via the thickness model and the measured value. Finally, the behavior of the corrected thermal diffusivities of the mono- and four-layered coatings, seen in Fig. 7(a), depends on the correction model. When using the two-layers adiabatic model, the thermal diffusivities of the mono- and four-layered coatings decrease from 0.28 mm^2/s at room temperature to, respectively, 0.21 and 0.19 mm^2/s at 1000 °C. However, the response signal of the experimental data deviates from this adiabatic model from 400 °C, where the two-layers heat loss and contact resistance model presents a better fitting. The thermal diffusivities

of the mono- and four-layered coatings reach then a minimum of, respectively, 0.26 and 0.24 mm^2/s at 300 °C, before further increasing to 0.39 and 0.33 mm^2/s at 1000 °C. Even though this increase of thermal diffusivities from 400 °C is unexpected and unclear, the thermal diffusivities of both coatings are similar at low temperatures and remain low independent of the chosen model. Moreover, the four-layered coating exhibits a lower thermal diffusivity compared to the monolayered coating.

Thermal conductivity of the coatings

The thermal conductivities of the mono- and four-layered coatings were calculated using Eq. (2), and the following heat capacity and linear thermal expansion of bulk lanthanum zirconate given in the literature [33; 34]:

$$C_{P[J/kg\cdot K]}(T_{[K]}) = 0.3742_{[J/kg\cdot K]} + 1.9179*10^{-4}_{\left[J/kg\cdot K^2\right]} T_{[K]} - 2.9453*10^{-8}_{\left[J/kg\cdot K^3\right]} T_{[K]}^{\ 2} \quad (7)$$

$$\alpha_{L[nm]}(T_{[K]}) = 1.0768_{[nm]} + 9.1805*10^{-6}_{[nm/K]} T_{[K]} + 4.1621*10^{-10}_{\left[nm/K^2\right]} T_{[K]}^{\ 2} + \frac{0.0423_{[nm\cdot K]}}{T_{[K]}}. \quad (8)$$

The thermal conductivities of the mono- and four-layered coatings, shown in Fig. 7(b), increase from, respectively, 0.16 and 0.21 W/(m·K) at room temperature to 0.32 and 0.34 W/(m·K) at 1000 °C when using the two-layers heat loss and contact resistance model, whereas they remain relatively constant around ~0.17 and 0.20 W/(m·K) for the two-layers adiabatic model. Despite the lower thermal diffusivity of the four-layered coating, the monolayer coating has a lower thermal conductivity because of the higher porosity.

4. Discussion

Two lanthanum zirconate coatings with different crack patterns were deposited. A monolayered coating was deposited and decomposed in a single step, and the decomposition of the thick green layer led to large crack spacings and crack openings. A multilayered coating was produced by successive deposition and decomposition of multiple thinner layers. Due to the small thickness of the individual layers, the resulting coating demonstrated small crack spacing and crack opening according to a model developed elsewhere [23].

The crystallized lanthanum zirconate four-layered coatings had smaller nanoparticles, a higher density, a higher hardness, a lower thermal diffusivity, and a higher thermal conductivity compared to crystallized monolayered coatings of similar thickness. The large porosity of the coatings is imputed to the large volume represented by the cracks. The porosity within the islands of the coatings was estimated by image analysis of SEM micrographs for a monolayered coating to be ~32 %. Because the cracks were partially filled during the deposition of multilayered coatings, these coatings exhibited a higher density of ~8 % compared to monolayered coatings relative to the theoretical density. The increased density strengthened the multilayered coatings and hence resulted in a higher hardness leading to self-healing. Besides, the large crack openings of the monolayered coating enable rapid diffusion of air into the coating, which promotes heat conduction. This phenomenon explains the lower thermal diffusivity of the multilayered coatings, because of the smaller crack opening and the fact that the cracks within individual layers do not necessarily connect through the entire thickness of the coatings.

Nevertheless, the benefits of the small crack openings are compensated by the higher density of the coatings, which results in a higher thermal conductivity.

The porosity within the islands of both mono- and multilayered coatings is mainly constituted of horizontal pores in the direction perpendicular to the heat flux, which is beneficial to decrease the thermal conductivities of the coatings. State-of-the-art YSZ TBCs have typical thermal conductivities of 0.8 to 1.7 W/(m·K) and 1.5 to 2.0 W/(m·K) for coatings deposited by APS and EBPVD, respectively [3], well above the values of 0.16 to 0.35 W/(m·K) reported in this study for lanthanum zirconate coatings deposited by spray pyrolysis. The large difference in thermal conductivities is proposed to be due to the low density of the deposited coatings, the nanostructure of the coatings, and the $La_2Zr_2O_7$ material, which has a lower thermal conductivity than YSZ.

Chen at al. [35] reported thermal conductivities of 0.73 to 0.79 W/(m·K) measured by the laser flash method for lanthanum zirconate coatings deposited by APS. The thermal conductivity was further reduced to ~0.42 W/(m·K) by using amorphous feedstock, due to a more uniform microstructure of the coatings and a higher porosity associated with the formation of nanopores [36]. Even though the given values are quite low compared to typical TBCs, they are higher than those reported in this study, mainly because of the difference in porosity between the coatings. The lanthanum zirconate coatings deposited by APS had a density ~5.5 $g \cdot cm^{-3}$ compared to densities of, respectively, 1.6 and 2.0 $g \cdot cm^{-3}$ for the mono- and four-layered coatings deposited by spray pyrolysis.

The deposition of thick and porous yttria-partially stabilized zirconia coatings by spraying nitrate solution in a low pressure plasma reactor revealed the presence of vertical cracks, and a total micro- and nano-porosity of 50 % [37]. The thermal diffusivity of such coatings was measured by the CO_2 laser technique and decreased

from ~0.15 mm^2/s at room temperature to ~0.09 mm^2/s at 1200 °C [38], which represents about one third of the values obtained from plasma sprayed material [39] and from the spray pyrolysis deposition of mono- and multi-layered coatings reported here. The lower thermal diffusivities were attributed to the finer nanostructure of the coatings and to the larger amount of porosity in the direction normal to the heat flux. In addition, thinner vertical cracks were formed in coatings deposited via the low pressure plasma technique compared to coatings produced by spray pyrolysis, which delayed the diffusion of the hot gas within the coatings.

Finally, even though the four-layered coating deposited by spray pyrolysis exhibited higher thermal conductivities than the monolayered coating, the lower thermal diffusivity, the higher hardness, the smaller features in the nanostructure, and the unique crack pattern of the multilayered coatings are more attractive properties for commercial applications. The low thermal conductivity and the ease of fabrication of such promising multilayered coatings by spray pyrolysis are of special interest for TBC applications.

5. Conclusion

The crystallization behavior of lanthanum zirconate coatings deposited by spray pyrolysis from an aqueous nitrate based precursor solution was investigated, and crystalline coatings were obtained from 700 °C. Heat-treated mono- and multi-layered coatings with different crack patterns prepared by spray pyrolysis were porous and nanocrystalline with particles of size, respectively, ~20 and ~15 nm and a thickness ~200 μm. The four-layered coatings demonstrated a higher density, a higher hardness, lower thermal diffusivities, and higher thermal conductivities compared to crystalline

monolayered coatings of similar thickness. The properties of the multilayered coatings are especially desirable for commercial applications and attributed to the crack pattern with smaller crack spacing and crack opening. Finally, the larger porosity of both coatings reduced the thermal conductivity to the range of 0.16 to 0.34 W/(m·K), which is lower compared to nanostructured lanthanum zirconate coatings deposited by APS.

Acknowledgement

Financial support from NTNU (Strategic area of Materials) is acknowledged.

References

[1] R. A. Miller. Thermal barrier coatings for aircraft engines: History and directions. J. Therm. Spray Technol. 1997;6:35-42.

[2] R. A. Miller. Current status of thermal barrier coatings - An overview. Surf. Coat. Technol. 1987;30:1-11.

[3] N. P. Padture, M. Gell, and E. H. Jordan. Thermal barrier coatings for gas-turbine engine applications. Science 2002;296:280-4.

[4] X. Q. Cao, R. Vassen, and D. Stoever. Ceramic materials for thermal barrier coatings. J. Eur. Ceram. Soc. 2004;24:1-10.

[5] R. Vassen, M. O. Jarligo, T. Steinke, D. E. Mack, and D. Stöver. Overview on advanced thermal barrier coatings. Surf. Coat. Technol. 2010;205:938-42.

[6] Y. Moriya and A. Navrotsky. High-temperature calorimetry of zirconia: Heat capacity and thermodynamics of the monoclinic-tetragonal phase transition. J. Chem. Thermodyn. 2006;38:211-23.

[7] R. Vassen, X. Q. Cao, F. Tietz, D. Basu, and D. Stover. Zirconates as new materials for thermal barrier coatings. J. Am. Ceram. Soc. 2000;83:2023-8.

[8] U. Schulz, B. Saruhan, K. Fritscher, and C. Leyens. Review on advanced EB-PVD ceramic topcoats for TBC applications. Int. J. Appl. Ceram. Technol. 2004;1:302-15.

[9] D. E. Wolfe, J. Singh, R. A. Miller, J. I. Eldridge, and D.-M. Zhu. Tailored microstructure of EB-PVD 8YSZ thermal barrier coatings with low thermal conductivity and high thermal reflectivity for turbine applications. Surf. Coat. Technol. 2005;190:132-49.

[10] H. Zhou, F. Li, B. He, J. Wang, and B.-d. Sun. Air plasma sprayed thermal barrier coatings on titanium alloy substrates. Surf. Coat. Technol. 2007;201:7360-7.

[11] F. Cernuschi, P. Bison, and A. Moscatelli. Microstructural characterization of porous thermal barrier coatings by laser flash technique. Acta Mater. 2009;57:3460-71.

[12] M. Karger, R. Vassen, and D. Stöver. Atmospheric plasma sprayed thermal barrier coatings with high segmentation crack densities: Spraying process, microstructure and thermal cycling behavior. Surf. Coat. Technol. 2011;206:16-23.

[13] M. Madhwal, E. H. Jordan, and M. Gell. Failure mechanisms of dense vertically-cracked thermal barrier coatings. Mater. Sci. Eng., A 2004;384:151-61.

[14] R. S. Lima and B. R. Marple. Nanostructured YSZ thermal barrier coatings engineered to counteract sintering effects. Mater. Sci. Eng., A 2008;485:182-93.

[15] N. P. Padture, K. W. Schlichting, T. Bhatia, A. Ozturk, B. Cetegen, E. H. Jordan, et al. Towards durable thermal barrier coatings with novel microstructures deposited by solution-precursor plasma spray. Acta Mater. 2001;49:2251-7.

[16] M. Gell, E. Jordan, M. Teicholz, B. Cetegen, N. Padture, L. Xie, et al. Thermal Barrier Coatings Made by the Solution Precursor Plasma Spray Process. J. Therm. Spray Technol. 2008;17:124-35.

[17] A. Feuerstein, J. Knapp, T. Taylor, A. Ashary, A. Bolcavage, and N. Hitchman. Technical and economical aspects of current thermal barrier coating systems for gas turbine engines by thermal spray and EBPVD: A review. J. Therm. Spray Technol. 2008;17:199-213.

[18] J. Karthikeyan, C. C. Berndt, J. Tikkanen, S. Reddy, and H. Herman. Plasma spray synthesis of nanomaterial powders and deposits. Mater. Sci. Eng., A 1997;238:275-86.

[19] P. S. Patil. Versatility of chemical spray pyrolysis technique. Mater. Chem. Phys. 1999;59:185-98.

[20] D. Beckel, A. Dubach, A. R. Studart, and L. J. Gauckler. Spray pyrolysis of $La_{0.6}Sr_{0.4}Co_{0.2}Fe_{0.8}O_{3-\delta}$ thin film cathodes. J. Electroceram. 2006;16:221-8.

[21] C. Agashe, M. G. Takwale, B. R. Marathe, and V. G. Bhide. Structural properties of SnO_2: F films deposited by spray pyrolysis. Sol. Energy Mater. 1988;17:99-117.

[22] S. B. Weber, H. L. Lein, T. Grande, and M.-A. Einarsrud. Deposition mechanisms of thick lanthanum zirconate coatings by spray pyrolysis. J. Am. Ceram. Soc. 2011;94:4256-62.

[23] S. B. Weber, T. Grande, G. W. Scherer, and M.-A. Einarsrud. Crack engineering in thick coatings prepared by spray pyrolysis deposition. J. Am. Ceram. Soc. 2013;96:420-8.

[24] J. Sniezewski, Y. LeMaoult, P. Lours, L. Pin, V. M. Bekale, D. Monceau, et al. Sol-gel thermal barrier coatings: Optimization of the manufacturing route and durability under cyclic oxidation. Surf. Coat. Technol. 2010;205:1256-61.

[25] W. J. Parker, R. J. Jenkins, C. P. Butler, and G. L. Abbott. Flash method of determining thermal diffusivity, heat capacity, and thermal conductivity. J. Appl. Phys. 1961;32:1679-84.

[26] J. Hartmann, O. Nilsson, and J. Fricke. Thermal Diffusivity Measurements on Two-Layered and Three-Layered Systems with the Laser-Flash Method. High Temp. - High Pressures 1993;25:403-10.

[27] L. M. Clark III and R. E. Taylor. Radiation loss in the flash method for thermal diffusivity. J. Appl. Phys. 1975;46:714-9.

[28] J. A. Cape and G. W. Lehman. Temperature and finite pulse-time effects in the flash method for measuring thermal diffusivity. J. Appl. Phys. 1963;34:1909-13.

[29] F. L. Yaggee, E. R. Gilbert, and J. W. Styles. Thermal expansivities, thermal conductivities, and densities of vanadium, titanium, chromium and some vanadium-base alloys: A comparison with austenitic stainless steel. J. Less-Common Met. 1969;19:39-51.

[30] K. C. Mills, S. U. Yuchu, L. I. Zushu, and R. F. Brooks. Equations for the calculation of the thermo-physical properties of stainless steel. ISIJ Int. 2004;44:1661-8.

[31] R. C. Heckman. Finite pulse-time and heat-loss effects in pulse thermal diffusivity measurements. J. Appl. Phys. 1973;44:1455-60.

[32] T. Y. R. Lee, A. B. Donaldson, and R. E. Taylor. Therm. Conduct. 1978;15:135-48.

[33] H. Zhou and D. Yi. Effect of rare earth doping on thermo-physical properties of lanthanum zirconate ceramic for thermal barrier coatings. J. Rare Earths 2008;26:770-4.

[34] S. Yamazaki, T. Yamashita, T. Matsui, and T. Nagasaki. Thermal expansion and solubility limits of plutonium-doped lanthanum zirconates. J. Nucl. Mater. 2001;294:183-7.

[35] H. Chen, Y. Gao, S. Tao, Y. Liu, and H. Luo. Thermophysical properties of lanthanum zirconate coating prepared by plasma spraying and the influence of post-annealing. J. Alloys Compd. 2009;486:391-9.

[36] H. Chen, Y. Gao, H. Luo, and S. Tao. Preparation and Thermophysical Properties of $La_2Zr_2O_7$ Coatings by Thermal Spraying of an Amorphous Precursor. J. Therm. Spray Technol. 2011;20:1201-8.

[37] F. Rousseau, C. Fourmond, F. Prima, M. H. Vidal Serif, O. Lavigne, D. Morvan, et al. Deposition of thick and 50 % porous YpSZ layer by spraying nitrate solution in a low pressure plasma reactor. Surf. Coat. Technol. 2011;206:1621-7.

[38] C. Fourmond, G. Da Rold, F. Rousseau, C. Guyon, S. Cavadias, D. Morvan, et al. Characterisation of thermal barrier coatings and ultra high temperature

composites deposited in a low pressure plasma reactor. J. Eur. Ceram. Soc. 2011;31:2295-302.

[39] G. Bertrand, P. Bertrand, P. Roy, C. Rio, and R. Mévrel. Low conductivity plasma sprayed thermal barrier coating using hollow psz spheres: Correlation between thermophysical properties and microstructure. Surf. Coat. Technol. 2008;202:1994-2001.

Tables

Table 1. Thickness, crack spacing, and crack opening of decomposed and heat-treated mono- and four-layered lanthanum zirconate coatings deposited at 280 °C at a distance of 20 cm.

Number of layers	Decomposition temperature, °C	Heat treatment temperature, °C	Thickness, µm	Crack spacing, µm	Crack opening, µm
One	575	None	208.5 ± 14	339 ± 85	44 ± 13
Four	575	None	205 ± 17	72.5 ± 20	11 ± 6
One	575	1000	207 ± 10	248 ± 102	28 ± 15
Four	575	1000	201 ± 15	85 ± 24	15 ± 8

Table 2. Hardness of crystalline mono- and four-layered lanthanum zirconate coatings deposited at 280 °C at a distance of 20 cm, decomposed at 575 °C for 14 min, and heat-treated at 1000 °C for 2 h.

Number of layers	Load, N	Hardness, MPa
One	0.98	8.7 ± 2
Four	0.98	31.7 ± 6
One	1.96	14.3 ± 3
Four	1.96	31.1 ± 7

Figure captions

Fig. 1. SEM micrographs of the surface microstructure of decomposed lanthanum zirconate coatings heat-treated at 1200 °C for 2 h and deposited at a distance of 25 cm (a) at 240 °C and decomposed at 510 °C, (b) at 280 °C and decomposed at 540 °C, and at a distance of 20 cm (c) at 240 °C and decomposed at 540 °C, and (d) at 280 °C and decomposed at 575 °C.

Fig. 2. XRD diffractograms of lanthanum zirconate coatings deposited at a distance of 20 or 25 cm at 240 °C or 280 °C, decomposed at 510 °C, 540 °C, or 575 °C for 14 min, and heat-treated at 1200 °C for 2 h. (In the legend, M=Cr, Ni, Fe or mixtures thereof).

Fig. 3. In-situ HTXRD diffractograms of a lanthanum zirconate coating deposited at a distance of 25 cm at 240 °C. The coating was not exposed to any heat treatment prior to the analysis. (In the legend, M=Cr, Ni, Fe or mixtures thereof).

Fig. 4. SEM micrographs of the surface and the cross-section microstructures of a monolayered lanthanum zirconate coating deposited at a distance of 20 cm at 280 °C, (a) and (b) decomposed at 575 °C for 14 min, and (c) and (d) heat-treated at 1000 °C for 2 h. Insert: higher magnification of the cross-section microstructure.

Fig. 5. XRD diffractogram of mono- and four-layered lanthanum zirconate coatings deposited at a distance of 20 cm at 280 °C, decomposed at 575 °C for 14 min, and heat-treated at 1000 °C for 2 h.

Fig. 6. SEM micrographs of the surface and the cross-section microstructures of a four-layered lanthanum zirconate coating deposited at a distance of 20 cm at 280 °C, (a) and (b) decomposed at 575 °C for 14 min, and (c) and (d) heat-treated at 1000 °C for 2 h. Insert: higher magnification of the cross-section microstructure.

Fig. 7. (a) Thermal diffusivity and (b) thermal conductivity of crystalline lanthanum zirconate mono- and four-layered coatings as a function of temperature.

Figures

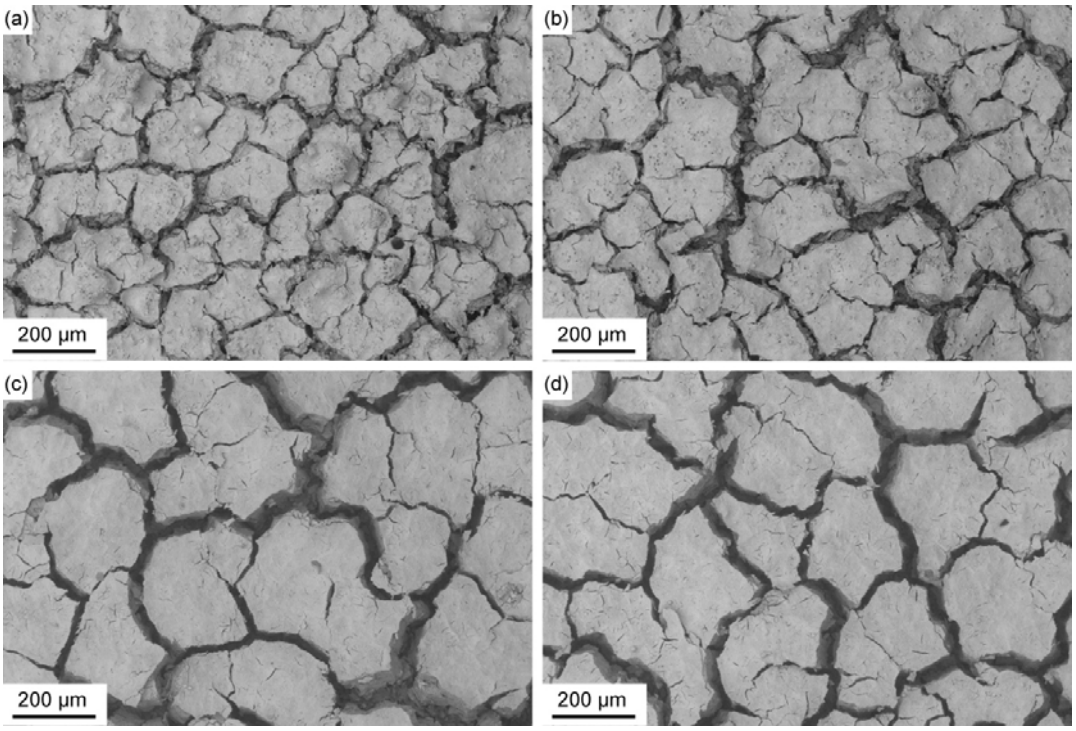

Fig. 1. SEM micrographs of the surface microstructure of decomposed lanthanum zirconate coatings heat-treated at 1200 °C for 2 h and deposited at a distance of 25 cm (a) at 240 °C and decomposed at 510 °C, (b) at 280 °C and decomposed at 540 °C, and at a distance of 20 cm (c) at 240 °C and decomposed at 540 °C, and (d) at 280 °C and decomposed at 575 °C.

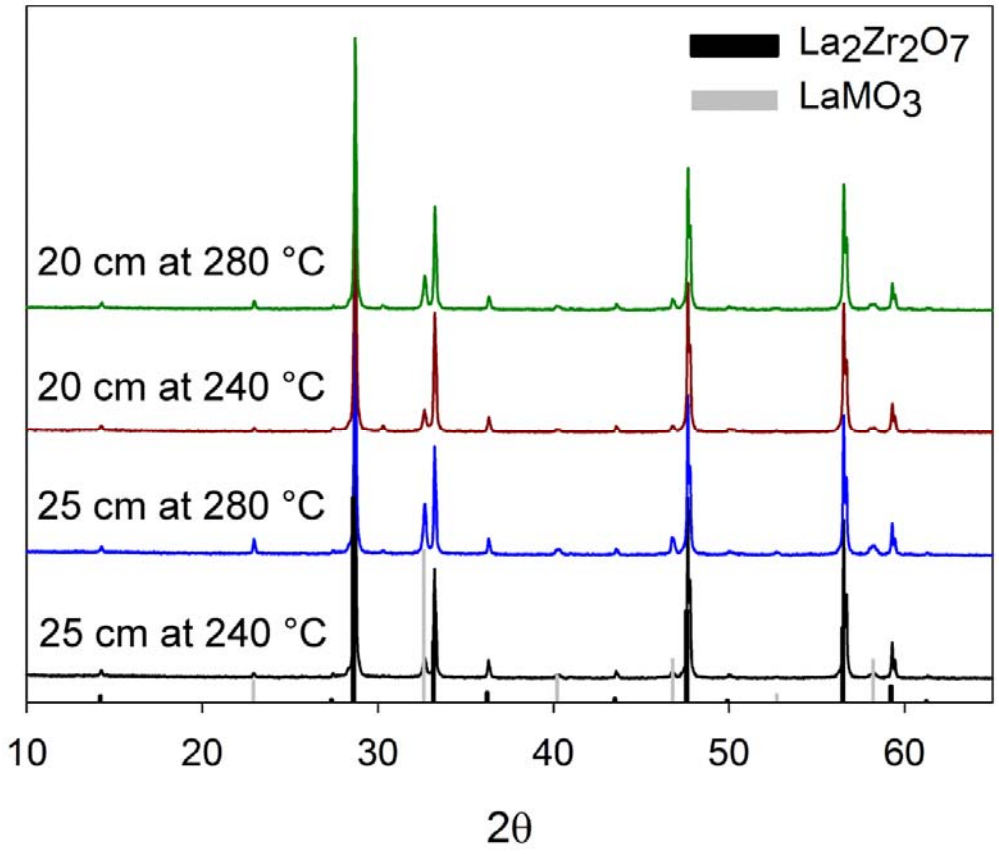

Fig. 2. XRD diffractograms of lanthanum zirconate coatings deposited at a distance of 20 or 25 cm at 240 °C or 280 °C, decomposed at 510 °C, 540 °C, or 575 °C for 14 min, and heat-treated at 1200 °C for 2 h. (In the legend, M=Cr, Ni, Fe or mixtures thereof).

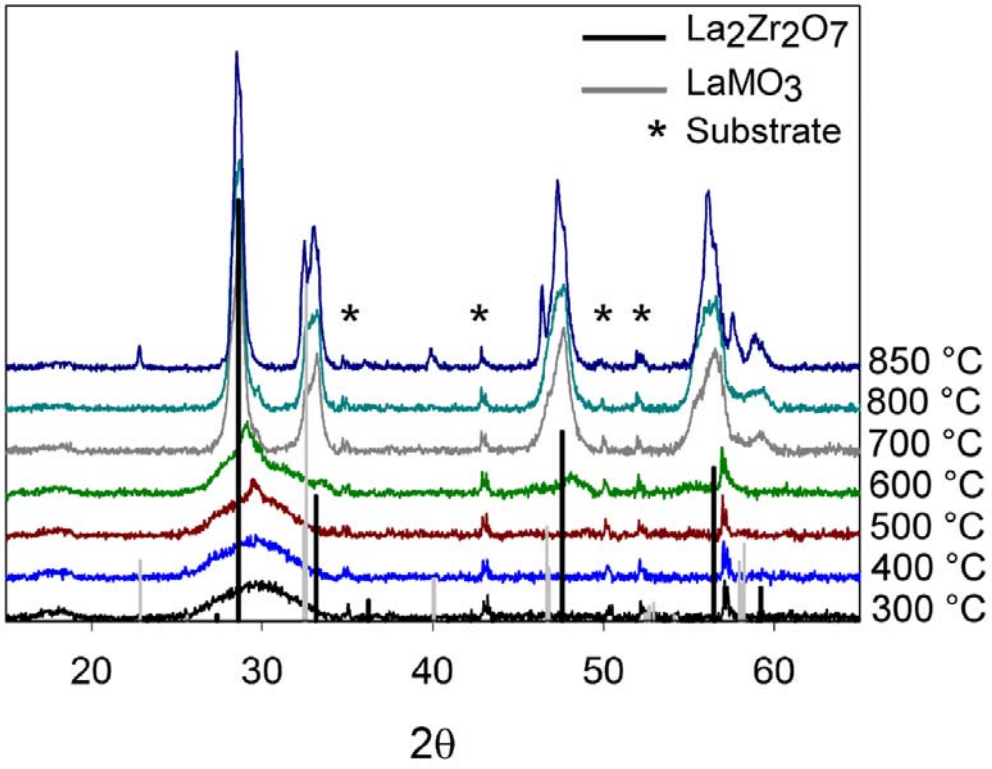

Fig. 3. In-situ HTXRD diffractograms of a lanthanum zirconate coating deposited at a distance of 25 cm at 240 °C. The coating was not exposed to any heat treatment prior to the analysis. (In the legend, M=Cr, Ni, Fe or mixtures thereof).

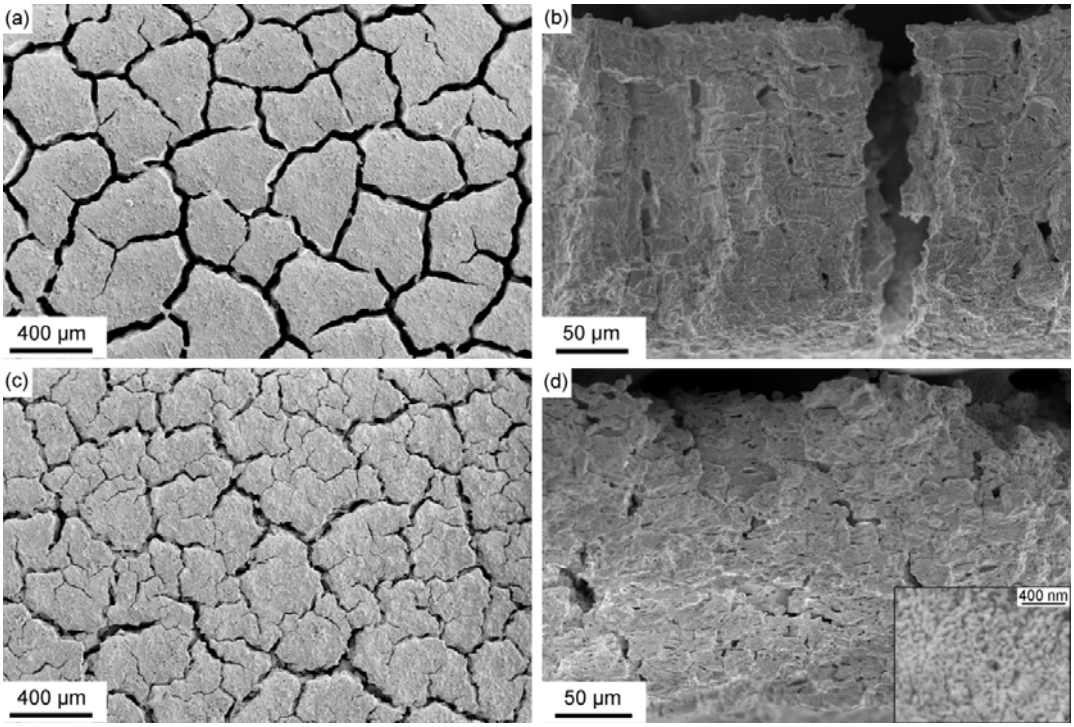

Fig. 4. SEM micrographs of the surface and the cross-section microstructures of a monolayered lanthanum zirconate coating deposited at a distance of 20 cm at 280 °C, (a) and (b) decomposed at 575 °C for 14 min, and (c) and (d) heat-treated at 1000 °C for 2 h. Insert: higher magnification of the cross-section microstructure.

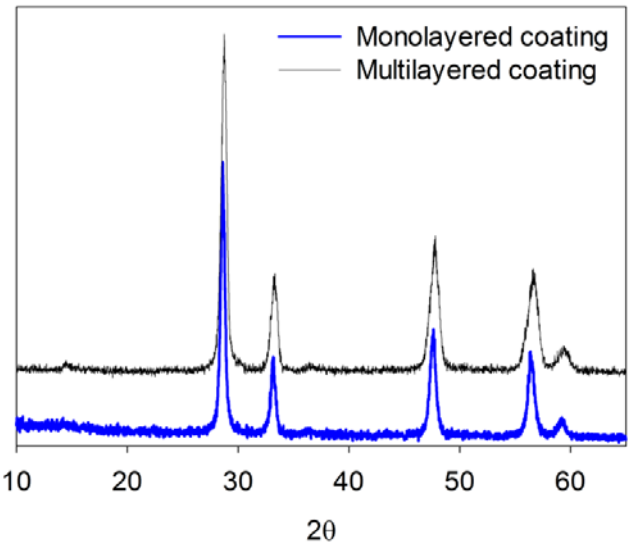

Fig. 5. XRD diffractogram of mono- and four-layered lanthanum zirconate coatings deposited at a distance of 20 cm at 280 °C, decomposed at 575 °C for 14 min, and heat-treated at 1000 °C for 2 h.

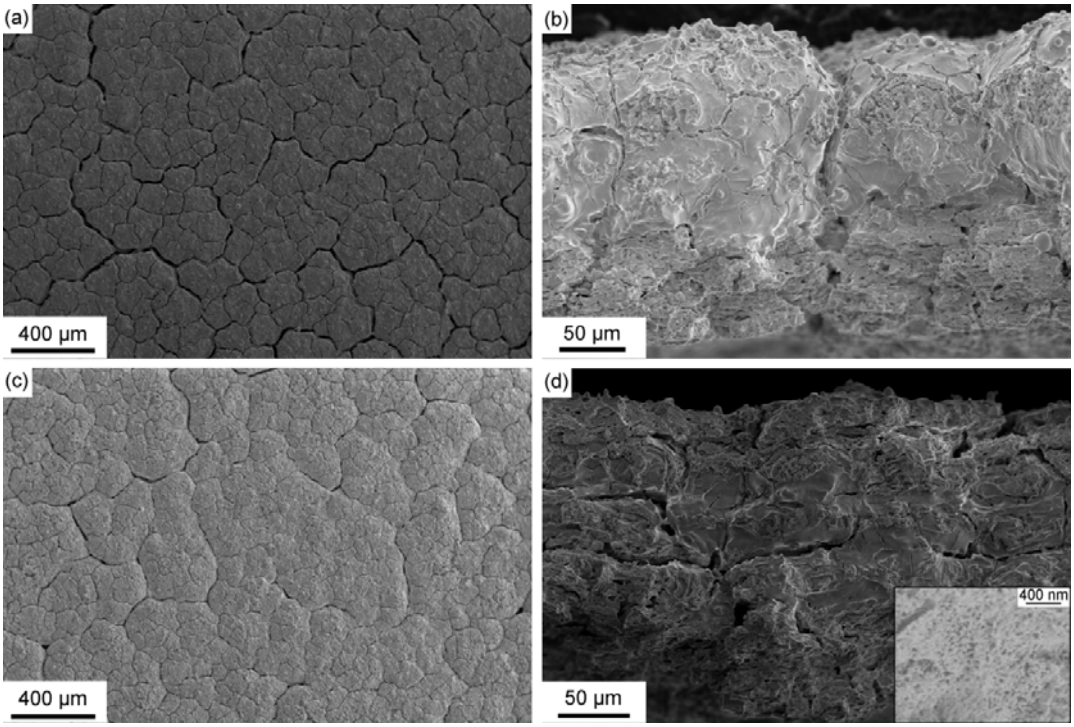

Fig. 6. SEM micrographs of the surface and the cross-section microstructures of a four-layered lanthanum zirconate coating deposited at a distance of 20 cm at 280 °C, (a) and (b) decomposed at 575 °C for 14 min, and (c) and (d) heat-treated at 1000 °C for 2 h. Insert: higher magnification of the cross-section microstructure.

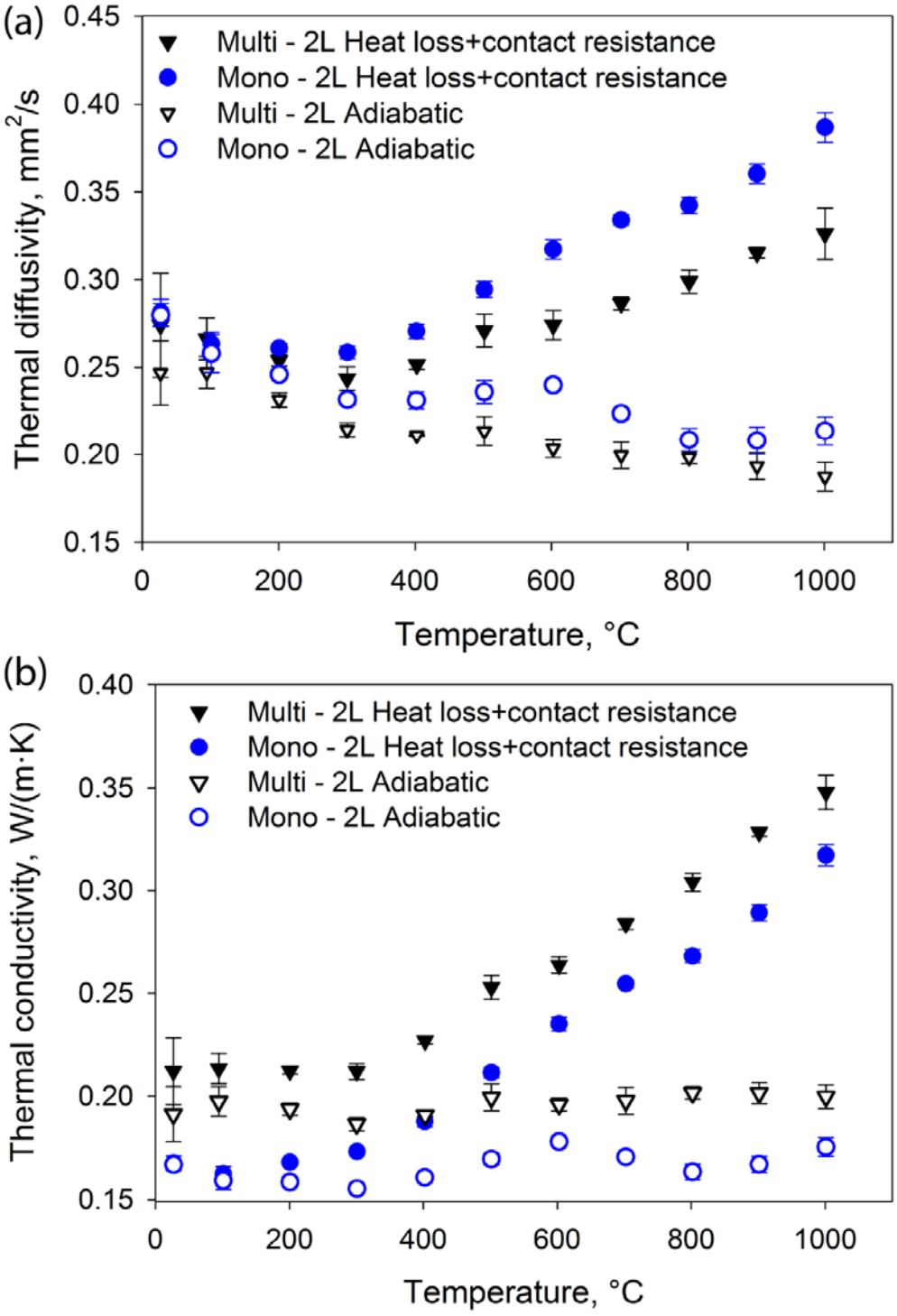

Fig. 7. (a) Thermal diffusivity and (b) thermal conductivity of crystalline lanthanum zirconate mono- and four-layered coatings as a function of temperature.